6-2012

Computationally efficient methods for modelling laser wakefield acceleration in the blowout regime

B. M. Cowan
Tech-X Corporation, Boulder, CO, benc@txcorp.com

Serguei Y. Kalmykov
University of Nebraska-Lincoln, s.kalmykov.2013@ieee.org

A. Beck
Katholieke Universiteit Leuven

X. Davoine
CEA, DAM, DIF, Arpajon, France

K. Bunkers
University of Nebraska-Lincoln

See next page for additional authors

J. Plasma Physics (2012), vol. 78, part 4, pp. 469–482. © Cambridge University Press 2012
doi:10.1017/S0022377812000517

Computationally efficient methods for modelling laser wakefield acceleration in the blowout regime

B. M. COWAN[1], S. Y. KALMYKOV[2], A. BECK[3,4], X. DAVOINE[3], K. BUNKERS[2], A. F. LIFSCHITZ[5], E. LEFEBVRE[3], D. L. BRUHWILER[1], B. A. SHADWICK[2] and D. P. UMSTADTER[2]

[1]Tech-X Corporation, 5621 Arapahoe Ave. Ste. A, Boulder, CO 80303, USA
(benc@txcorp.com)
[2]Department of Physics and Astronomy, University of Nebraska – Lincoln, NE 68588-0299, USA
[3]CEA, DAM, DIF, Arpajon F-91297, France
[4]Centrum voor Plasma-Astrofysica, Departement Wiskunde, KU Leuven, Celestijnenlaan 200B, B-3001 Leuven, Belgium
[5]Laboratoire d'Optique Appliquée, ENSTA, Ecole Polytechnique, CNRS, 91761 Palaiseau, France

(Received 15 Febuary 2012; accepted 23 April 2012; first published online 13 June 2012)

Abstract. Electron self-injection and acceleration until dephasing in the blowout regime is studied for a set of initial conditions typical of recent experiments with 100-terawatt-class lasers. Two different approaches to computationally efficient, fully explicit, 3D particle-in-cell modelling are examined. First, the Cartesian code VORPAL (Nieter, C. and Cary, J. R. 2004 VORPAL: a versatile plasma simulation code. *J. Comput. Phys.* **196**, 538) using a perfect-dispersion electromagnetic solver precisely describes the laser pulse and bubble dynamics, taking advantage of coarser resolution in the propagation direction, with a proportionally larger time step. Using third-order splines for macroparticles helps suppress the sampling noise while keeping the usage of computational resources modest. The second way to reduce the simulation load is using reduced-geometry codes. In our case, the quasi-cylindrical code CALDER-CIRC (Lifschitz, A. F. et al. 2009 Particle-in-cell modelling of laser-plasma interaction using Fourier decomposition. *J. Comput. Phys.* **228**(5), 1803–1814) uses decomposition of fields and currents into a set of poloidal modes, while the macroparticles move in the Cartesian 3D space. Cylindrical symmetry of the interaction allows using just two modes, reducing the computational load to roughly that of a planar Cartesian simulation while preserving the 3D nature of the interaction. This significant economy of resources allows using fine resolution in the direction of propagation and a small time step, making numerical dispersion vanishingly small, together with a large number of particles per cell, enabling good particle statistics. Quantitative agreement of two simulations indicates that these are free of numerical artefacts. Both approaches thus retrieve the physically correct evolution of the plasma bubble, recovering the intrinsic connection of electron self-injection to the nonlinear optical evolution of the driver.

1. Introduction

Relativistic Langmuir waves driven by short, intense laser pulses in rarefied plasmas maintain accelerating gradients several orders of magnitude higher than those accessible in conventional metallic structures (Tajima and Dawson 1979; Gorbunov and Kirsanov 1987; Esarey et al. 2009). The technical simplicity and compactness of these laser-plasma accelerators (LPAs) is attractive for a broad range of applications, such as nuclear activation and on-site isotope production (Leemans et al. 2001; Reed et al. 2007), long-distance probing of defects in shielded structures (Ramanathan et al. 2010), and testing radiation resistivity of electronic components (Hidding et al. 2011). Realization of compact, inexpensive, bright x- and gamma-ray sources using electron beams from LPAs (Rousse et al. 2004; Ta Phuoc et al. 2005; Rousse et al. 2007; Kneip et al. 2010; Cipiccia et al. 2011) holds the promise to enable a much wider user community than can be served by existing large-scale facilities. These applications are not especially demanding as regards electron beam quality, and in fact sometimes draw benefits from poor beam collimation and a broad energy spectrum (Hidding et al. 2011). However, there are also important applications with much tighter beam requirements. Such applications include generating coherent x-rays using an external magnetic undulator (Grüner et al. 2007; Schlenvoigt et al. 2008a,b; Fuchs et al. 2009), producing x-rays for phase contrast imaging (Fourmaux et al. 2011; Kneip et al. 2011), and high-brightness, quasi-monochromatic gamma-ray Compton sources (Leemans et al. 2005; Hartemann et al. 2007); these require electron beams

with a multi-kA current, low-phase space volume, and energy in the few gigaelectronvolt (GeV) range.

Achieving this high level of accelerator performance is a major near-term goal of the LPA community. Modern laser systems capable of concentrating up to 10 Joules of energy in a sub-50 femtosecond pulse (Yanovsky et al. 2008; Froula et al. 2009; Kneip et al. 2009; Fourmaux et al. 2011) make it possible to achieve the so-called blowout (or 'bubble') regime, which is desirable due to its technical simplicity and scalability (Gordienko and Pukhov 2005; Lu et al. 2007). In this regime, motion of electrons in the focus of the laser pulse is highly relativistic. The laser ponderomotive force expels plasma electrons from the region of the pulse, while the fully stripped ions remain essentially immobile, creating a column of positive charge in the laser wake. The charge separation force attracts bulk plasma electrons to the axis, creating a closed bubble devoid of electrons. This co-propagating electron density bubble (Rosenzweig et al. 1991; Mora and Antonsen 1996; Pukhov and Meyer-ter-Vehn 2002; Gordienko and Pukhov 2005; Lu et al. 2006) guides the laser pulse over many Rayleigh lengths (Mora and Antonsen 1996; Lu et al. 2007). The bubble readily traps initially quiescent background electrons, accelerating them to hundreds of megaelectronvolts (MeV) over a few millimeters, creating a collimated electron bunch (Pukhov and Meyer-ter-Vehn 2002; Kalmykov et al. 2011a). It is in this regime that the first quasi-monoenergetic electrons were produced from laser plasma interactions in the laboratory (Faure et al. 2004; Geddes et al. 2004; Mangles et al. 2004), and the GeV energy range was approached (Leemans et al. 2006; Karsch et al. 2007; Hafz et al. 2008; Froula et al. 2009; Kneip et al. 2009; Clayton et al. 2010; Liu et al. 2011; Lu et al. 2011; Pollock et al. 2011).

Multi-dimensional particle-in-cell (PIC) simulations have played a key role in understanding the physics of the fully kinetic, strongly relativistic blowout regime. The PIC method (Hockney and Eastwood 1981; Birdsall and Langdon 1985) self-consistently models both electromagnetic fields and charged particles, representing field quantities on a grid and particles in a continuous phase space. Given sufficient computing power, electromagnetic PIC codes can simulate the plasma electrons (and ions, if necessary), the laser pulse driving the plasma wake, and the dynamics of electrons injected into the accelerating potential. In particular, two- and three-dimensional PIC simulations have been essential in understanding the dynamical nature of the electron self-injection process (Xu et al. 2005; Oguchi et al. 2008; Kalmykov et al. 2009, 2010, 2011a, b; Wu et al. 2009; Zhidkov et al. 2010). However, to capture precisely the correlation between driver dynamics, electron self-injection, and GeV-scale acceleration in the bubble regime, a simulation must meet a number of challenging requirements.

Optimization of GeV-scale LPA performance, even with the use of massively parallel computation, is a challenging task, especially because of the necessary cm-scale laser-plasma interaction length. The laser energy is used most effectively if electrons are accelerated until they outrun the bubble and exit the accelerating phase, at which point they will have gained the maximum possible energy in an LPA stage,

$$E_d \approx 2.7\gamma_g^{4/3} P_{\mathrm{TW}}^{1/3}\,\mathrm{MeV}. \tag{1.1}$$

Acceleration to this *dephasing limit* occurs over the distance (Lu et al. 2007)

$$L_d \approx 0.6\lambda_0 \gamma_g^{8/3} P_{\mathrm{TW}}^{1/6}. \tag{1.2}$$

Here, P_{TW} is the laser power in terawatts (TW) ($1\,\mathrm{TW} = 10^{12}\,\mathrm{W}$), $\gamma_g = \omega_0/\omega_{\mathrm{pe}} \gg 1$ is the Lorentz factor associated with the linear group velocity of the pulse in plasma, ω_0 is the laser frequency, $\lambda_0 = 2\pi c/\omega_0$ is the laser wavelength, $\omega_{\mathrm{pe}} = (n_0 e^2/m_e \epsilon_0)^{1/2}$ is the electron Langmuir frequency, m_e is the electron rest mass, n_0 is the background electron density, e is the electron charge, and ϵ_0 is the permittivity of free space. The scalings (1.1) and (1.2) imply that the pulse remains self-guided, namely, it remains longer than $c\,\omega_{\mathrm{pe}}^{-1}$ (Sprangle et al. 1990; Gorbunov et al. 2005), and its power exceeds the critical power for relativistic self-focusing, $P_{\mathrm{cr}} = 16.2\gamma_g^2\,\mathrm{GW}$ (Sun et al. 1987). Increasing the electron energy therefore requires reduction of electron plasma density, increasing both the bubble velocity and size,

$$L_{\mathrm{acc}} \approx 0.9\lambda_0 \gamma_g^{2/3} P_{\mathrm{TW}}^{1/6}, \tag{1.3}$$

where L_{acc} is the length of the accelerating phase of the wakefield (roughly equal to the bubble radius). Electron dephasing scales as $L_d \sim n_0^{-4/3}$ and thus the final energy gain scales as $E_d \sim n_0^{-2/3}$. For instance, with a 200-TW pulse and a wavelength $\lambda_0 = 0.8\,\mu\mathrm{m}$, reaching 1-GeV energy needs a 0.47-cm length plasma with density $n_0 = 3.5 \times 10^{18}\,\mathrm{cm}^{-3}$. Doubling that energy would require nearly four times the plasma length and three times lower density, also increasing the bubble size by ~40%. Simulations of LPA commonly use a moving window, where the simulation box propagates with the speed of light colinearly with the laser pulse. This optimization notwithstanding, even the experiments with currently operating 100-TW systems bring forth the task of modelling the pulse propagation in cm-length plasmas, with the size of the 3D simulation box of the order of hundred(s) of microns longitudinally and transversely.

The greatest challenge arises from the great disparity of physical scales between the laser wavelength and plasma length, which is the hallmark of high-energy laser-plasma acceleration. The need to resolve the laser wavelength, $\lambda_0 \sim 1\,\mu\mathrm{m}$, fixes the grid resolution, and because of stability conditions (Courant et al. 1967) also limits the time step to a small fraction of ω_0^{-1}. Furthermore, the strong localization of the injection process imposes an even stricter limit on grid resolution; the vast majority of injection candidates are concentrated in the inner lining of the bubble (the sheath), and

penetrate into the bubble near its rear, where the sheath is longitudinally compressed to a few tens of nanometres (Wu et al. 2009; Kalmykov et al. 2011a). Resolving this structure, together with ensuring sufficient particle statistics in the sheath, is necessary to avoid excessive sampling noise and eliminate unphysical effects. In this situation, extending the plasma length to centimeters and increasing the size of the simulation window to hundreds of microns, while at the same time maintaining sufficient macroparticle statistics, would require solving Maxwell's equations on meshes amounting to billions of grid points, and advancing 1–10 billion macroparticles over millions of time steps. Performing such simulations with standard electromagnetic solvers and particle movers requires a national-scale supercomputing facility. As a result, an attempt to reproduce the long time-scale evolution of the laser and the bubble together with fine details of the electron self-injection dynamics is usually a compromise between affordable simulation load and unavoidable coarseness of results. However, the high precision of modern LPA experiments and high beam quality requirements of applications are rather unforgiving to these compromises and do not tolerate numerical artefacts (Cormier-Michel et al. 2008).

These considerations make it clear that PIC algorithms must be modified in order to reduce the required computational resources without compromising precision. One of the main directions is development of electromagnetic solvers that minimize numerical error while using the lowest possible grid resolution. One particular limitation of PIC that requires high longitudinal resolution is that of numerical dispersion. In PIC, electromagnetic fields are typically updated using the finite-difference time-domain (FDTD) method on a staggered Yee grid (Yee 1966; Taflove and Hagness 2005). This method is second-order accurate, and since it is explicit and local, it parallelizes efficiently, enabling large-scale simulations. However, it is known that this algorithm experiences numerical dispersion error for waves propagating along the axis, which leads to errors in the group velocity of the laser pulse. This artificial slowdown of the driver and the bubble leads to incorrect dephasing of accelerated electrons and also permits synchronization of sheath electrons with the bubble, leading to their unphysical injection. Mitigating this effect by using higher resolution increases the computation time quadratically. Because of the deleterious effects of numerical dispersion in FDTD schemes, efforts have been made to develop *perfect dispersion* algorithms, which exhibit no numerical dispersion for waves propagating along a grid axis. For accelerator applications, several modifications to FDTD have been described that correct for numerical dispersion using implicit methods (Zagorodnov et al. 2003; Zagorodnov and Weiland 2005). Since LPA simulations tend to be of quite large scale (using thousands of processor cores), an explicit algorithm is desirable for reasons of computational efficiency. Such an algorithm has been described in two dimensions (Pukhov 1999) and three dimensions for cubic cells (Kärkkäinen et al. 2006). These algorithms have been also explored for LPA as a means of reducing noise in boosted-frame simulations (Vay et al. 2011).

In this paper, we use two complementary simulation codes (with different numerical approaches and physics content) to explore physical phenomena involved in self-injection and acceleration of electrons until dephasing under typical conditions of recent experiments with 100-TW-class lasers. We use a newly developed perfect-dispersion algorithm (Cowan et al. in preparation) implemented in a fully explicit 3D Cartesian VORPAL simulation framework (Nieter and Cary 2004), subsequently referred to as VORPAL-PD. The algorithm, briefly described in Sec. 2, eliminates numerical dispersion in the direction of pulse propagation. Thus, even with a relatively large longitudinal grid spacing ($\sim$15 grid points per λ_0), the correct group velocity of a broad-bandwidth laser pulse is obtained.

The other code used here, CALDER-CIRC, uses cylindrical geometry. This code uses poloidal mode decomposition of fields and currents defined on a radial grid, while macroparticles retain their full 3D dynamics in Cartesian coordinates (Lifschitz et al. 2009). Well-preserved cylindrical symmetry of the laser-plasma interaction enables using just a few lower-order modes. Neglecting higher order, non-axisymmetric contributions to the wakefields and currents makes it possible to approach the performance of a 2D code. CALDER-CIRC thus allows for fast, extra high resolution runs with excellent macroparticle statistics (Kalmykov et al. 2010, 2011a, 2012).

The paper is organized as follows. In Sec. 2 we outline the main features of the recently implemented perfect dispersion algorithm in the VORPAL-PD code. Section 3 is dedicated to the benchmarking of VORPAL-PD against CALDER-CIRC. Section 4 summarizes the results and indicates the directions of future work.

2. The perfect dispersion method

In this section we give a brief overview of the perfect dispersion method we use; a more complete description together with detailed benchmarks will be presented in Cowan et al. (in preparation). Our method is based on that of Pukhov (1999) and Kärkkäinen et al. (2006), in which the FDTD algorithm is modified by smoothing the fields in curl operator in one of Maxwell's equations. We choose to smooth electric fields for the magnetic field update; our update equations are then

$$D_t \boldsymbol{B} = -\nabla' \times \boldsymbol{E}, \quad D_t \boldsymbol{E} = c^2 \nabla \times \boldsymbol{B} - \frac{\boldsymbol{J}}{\epsilon_0}, \qquad (2.1)$$

where $\boldsymbol{J}$ is the electric current deposited from particle motion. Here D_t is the finite difference time derivative, $\nabla\times$ is the standard finite difference curl operator, and $\nabla'\times$ is the modified curl operator. Our modification to

the curl operator involves applying smoothing transverse to the coordinate axis along which the derivative is taken. For instance, when computing $\partial E_y/\partial x$, E_y is smoothed in the y and z directions. This is equivalent to applying a smoothing operator before the numerical derivative operator. The electric field is smoothed only for the update of the magnetic field; the smoothed fields are not stored for the next time step.

The smoothed curl operator $\nabla' \times$ is formed by modifying the finite difference operation. If D_i is the numerical derivative operator in the ith direction, then for the modified curl we use $D_i S_i$ in place of D_i, where S_i is the smoothing operator for the derivative. The smoothing operator S_x is defined by the stencil in y and z directions

$$\begin{bmatrix} \gamma_{yz} & \beta_z & \gamma_{yz} \\ \beta_y & \alpha_x & \beta_y \\ \gamma_{yz} & \beta_z & \gamma_{yz} \end{bmatrix}, \tag{2.2}$$

and similar relations hold for cyclic permutations of coordinate indices. The coefficients α_i, β_i, and γ_{ij} are chosen to guarantee that waves propagating along the x-axis (the laser propagation direction in our simulations) in vacuum experience no numerical dispersion as described in Cowan et al. (in preparation). The only constraint is that the longitudinal grid spacing Δx must satisfy $\Delta x \leqslant \Delta y, \Delta z$ for the transverse grid spacings Δy and Δz.

3. Benchmarking

While a technological path to high-quality GeV beams exists, experimental progress is impeded by an incomplete understanding of the intrinsic relation between electron self-injection and nonlinear optical evolution of the driver, and hence by the lack of suitable criteria for the selection of optimal regimes that produce beams with the smallest possible phase-space volume. Control and optimization of the fully kinetic, intrinsically 3D process of electron self-injection is a daunting task. It involves a systematic study of the links among the dynamics of self-injection and the nonlinear optical processes involving the laser pulse and the bubble.

Because of the extended acceleration length, the interaction of the laser pulse with the plasma is rich in nonlinear phenomena. Even a Gaussian beam which is perfectly matched to the electron density gradient in which it propagates is not immune to nonlinear optical processes. Oscillations of the pulse spot size because of nonlinear refraction (Oguchi et al. 2008; Kalmykov et al. 2010; Zhidkov et al. 2010), self-phase modulation leading to the formation of a relativistically intense optical piston (Tsung et al. 2002; Lontano and Murusidze 2003; Faure et al. 2005; Pai et al. 2010; Vieira et al. 2010; Kalmykov et al. 2011*a*,*b*, 2012), and relativistic filamentation (Andreev et al. 2007; Thomas et al. 2007; Thomas et al. 2009) are processes that result in pulse deformations. Electron self-injection appears to be extremely sensitive to such changes in pulse shape, which lead to the contamination of the electron beam by polychromatic, poorly collimated background (Kalmykov et al. 2011b, 2012). Such contamination is readily seen even in simulations with idealized initial conditions (Froula et al. 2009; Kneip et al. 2009; Kalmykov et al. 2010; Martins et al. 2010; Kalmykov et al. 2011a, 2012). The complicated modal structure of incident pulse further aggravates the situation, leading to continuous off-axis injection, collective betatron oscillations (Glinec et al. 2008; Mangles et al. 2009; Cummings and Thomas 2011), and electron beam steering (Popp et al. 2010). In practice, these phenomena currently preclude operation reliable enough to enable high-precision user experiments; reported islands of stability for self-injection in laser and plasma parameter space remain relatively narrow (Karsch et al. 2007; Mangles et al. 2007; Thomas et al. 2007; Hafz et al. 2008; Maksimchuk et al. 2008; Wiggins et al. 2010). Numerical codes used in predictive modelling of LPAs must be able to reproduce these phenomena with high precision in order not to confuse the instability of acceleration caused by physical processes with unphysical artefacts caused by intrinsic deficiencies of numerical algorithms, such as numerical dispersion, high sampling noise, and grid heating.

3.1. Simulation parameters

The simulations presented here extend the earlier case study by Kalmykov et al. (2011a) and use the same set of initial conditions. A transform-limited Gaussian laser pulse with full width at half-maximum (FWHM) in intensity $\tau_L = 30\,\text{fs}$, wavelength $\lambda_0 = 0.805\,\mu\text{m}$, and 70-TW power is focussed at the plasma border ($x = 0$) into a spot size $r_0 = 13.6\,\mu\text{m}$, and propagates in the positive x-direction. The laser pulse is polarized in the y-direction. The peak intensity at the focus is $2.3 \times 10^{19}\,\text{W/cm}^2$, giving a normalized vector potential of $a_0 = 3.27$. The plasma density has a 0.5-mm linear entrance ramp followed by a 2-mm plateau and a 0.5-mm linear exit ramp. The density in the plateau region, $n_0 = 6.5 \times 10^{18}\,\text{cm}^{-3}$, corresponds to $\gamma_g \approx P/P_{\text{cr}} \approx 16.3$ and dephasing length $L_d \approx 1.7\,\text{mm}$.

The simulations carried out with VORPAL-PD use grid spacings of $\Delta x = 0.06\lambda_0 = 48.3\,\text{nm}$ longitudinally and $\Delta y = \Delta z = 0.5\lambda = 403\,\text{nm}$ transversely, with four macroparticles per cell. Use of third-order splines for macroparticle shapes reduces the sampling noise, mitigating the adverse effect of the coarse grid. The domain in the VORPAL-PD simulations is 72 μm long and 91 μm wide, and is surrounded transversely by a 16-layer perfectly matched layer absorbing boundary. The code is fully parallelized, and was run using 6144 cores on the Hopper supercomputer at the National Energy Research Scientific Computing Center (NERSC). Completion of a typical run took $\sim 3 \times 10^5$ CPU hours.

The CALDER-CIRC simulation uses 45 macroparticles per cylindrical cell, formed by the revolution of the grid

cell around the propagation axis. The longitudinal grid spacing is $\Delta x = 0.125c/\omega_0 \approx 16\,\text{nm}$. The aspect ratio $\Delta r/\Delta x = 15.6$ (where $r = \sqrt{y^2 + z^2}$), and the time step $\Delta t = 0.1244\omega_0^{-1}$. With these grid parameters, numerical dispersion is negligible, and the sampling noise is significantly reduced. This high resolution simulation does not indicate any new physical effects compared to the VORPAL-PD simulation, and does not exhibit significant differences in quantitative results. Well-preserved cylindrical symmetry during the interaction (confirmed in the VORPAL-PD simulation) enables us to approximate fields and currents using just the two lowest order poloidal modes, thus reducing the 3D problem to an essentially 2D one. These results confirm the earlier established fact (Lifschitz et al. 2009) that in the case of a linearly polarized laser, higher order modes contribute only weakly to the electric field. Comparison with the results of the VORPAL-PD runs shows that our restriction to only two modes is sufficiently precise to reproduce all relevant physical effects, and to simulate the propagation through a 3-mm plasma in 2 625 CPU hours on 250 cores.

3.2. Formation of quasi-monoenergetic bunches and physical origin of dark current

Upon entering the plasma, the strongly overcritical pulse rapidly self-focuses, reaching its highest intensity at $x \approx 0.8\,\text{mm}$, soon after entering the density plateau. Full blowout is maintained over the entire propagation distance. In both simulations, electrons are accelerated until dephasing in two distinct stages, each characterized by completely different laser pulse dynamics. *Transverse* evolution of the laser pulse is the hallmark of Stage I. The pulse spot size oscillates, first causing expansion and then contraction of the bubble. The bubble expansion produces self-injection of electrons from the sheath; stabilization and contraction of the bubble extinguish injection, limiting the beam charge to a fraction of a nC. Phase space rotation creates a well-collimated quasi-monoenergetic bunch long before dephasing. Further acceleration (Stage II) is dominated by *longitudinal (temporal)* self-compression of the pulse, leading to gradual elongation of bubble and continuous injection, producing a polychromatic, poorly collimated energy tail – known as *dark current* – with a few nC charge. This two-stage evolution has been noticed in earlier simulations (Froula et al. 2009; Kneip et al. 2009), and explained in detail in Kalmykov et al. (2011a,b, 2012).

The correlation between the plasma bubble evolution and the self-injection process is quantified in Fig. 1. Panel (a) shows the length of the accelerating phase on axis, viz. the length of the region inside the bubble where the longitudinal electric field is negative. Panel (b) shows the longitudinal 'collection phase space,' viz. momenta of macroparticles reaching the dephasing point, $p_x(x = x_{\text{deph}})$, versus their initial position in plasma. Panel (c) shows the collection volume: the initial positions of electrons reaching the dephasing point. (The same quantities were used by Kalmykov et al. (2012) to evaluate the role of beam loading in the self-injection process.) Comparison of these three panels shows that *electrons are injected only during the periods of bubble expansion.*

During Stage I, radial oscillation of the laser pulse tail inside the bubble causes alternating expansion and contraction of the first bucket, clearly seen in the progression from $x = 0.6$ to 1.24 mm in Fig. 1(a). The bubble size oscillates around the average value predicted by the estimate (1.3), $L_{\text{acc}} \approx 9.5\,\mu\text{m}$. Electron self-injection into the oscillating bubble leads to the formation of a quasi-monoenergetic component in the energy spectrum. At the end of Stage I, at $x \approx 1.24\,\text{mm}$, the bubble contracts to the same size in both runs, truncating the tail of injected bunch and expelling electrons injected between $x = 0.825$ and 0.95 mm. These electrons do not reach dephasing and thus are missing in Figs. 1(b) and (c). Electrons injected between $x = 0.65$ and 0.825 mm remain in the bubble and are further accelerated. This well-separated group of particles is clearly seen in Fig. 1(b). In both the VORPAL-PD and CALDER-CIRC simulations, these electrons reach dephasing first, preserving low-energy spread, and are accelerated to the highest energy, $E \approx 500\,\text{MeV}$. The bubble expands more rapidly and stabilizes sooner in the VORPAL-PD simulation, causing stronger reduction of phase velocity in subsequent buckets (second and third). Hence, in contrast with the CALDER-CIRC run, VORPAL-PD gives a noticeable amount of charge trapped and pre-accelerated in these buckets. These electrons, indicated by red ellipse in Fig. 1(b), are swallowed by the expanding first bucket during Stage II and are further accelerated, contributing to a dark current. This contribution, however, appears to be fairly minimal in comparison to the amount of continuously injected charge during Stage II.

The leading edge of the laser pulse constantly experiences a negative gradient of the nonlinear index of refraction. As a result, by the end of Stage I, it accumulates considerable red-shift. During Stage II, plasma-induced group velocity dispersion slows the red-shifted spectral components relative to the unshifted components, leading to front etching and pulse self-compressing into a relativistically intense, few cycle long optical piston (Tsung et al. 2002; Lontano and Murusidze 2003; Faure et al. 2005; Kalmykov et al. 2011a). As the pulse transforms into a piston, the bubble constantly elongates, resulting in copious trapping and creating a poorly collimated, polychromatic tail, clearly seen in Fig. 1(b). At the dephasing point, $x_{\text{deph}} \approx 2.4\,\text{mm}$, the bubble size becomes nearly twice the estimate $L_{\text{acc}} \approx 9.5\,\mu\text{m}$ based on the scaling law (1.3). Even though Fig. 1(a) shows a larger bubble expansion in the VORPAL-PD run, the sections of collection phase space corresponding to Stage II look nearly identical for both codes in Fig. 1(b). Notably, beam loading provides only a minor contribution to bubble expansion, and is thus not a dominant cause of continuous injection (Kalmykov et al. 2012).

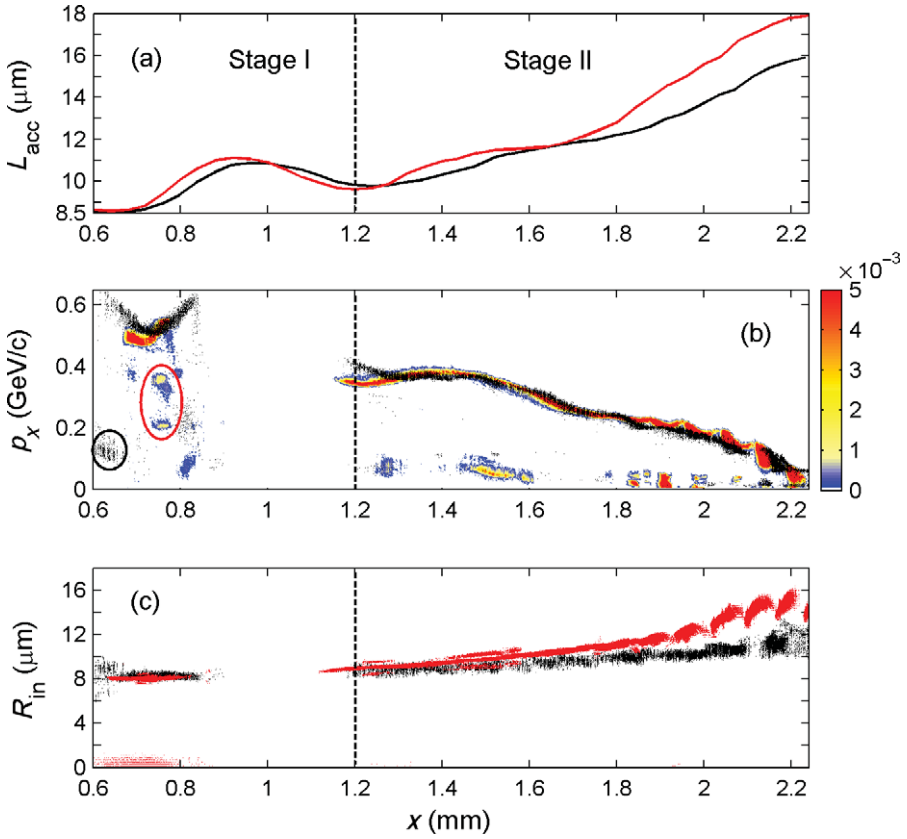

Figure 1. (Colour online) (a) Length of the accelerating phase vs. propagation distance in CALDER-CIRC (black) and VORPAL-PD simulations (red/grey). Expansion and contraction of the bubble because of nonlinear focusing of the driver (Stage I) is followed by continuous expansion caused by pulse self-compression (Stage II). (b) Longitudinal momentum of electrons reaching the dephasing point, $x_{deph} \approx 2.4$ mm, vs. their initial longitudinal positions. Black dots are the CALDER-CIRC macroparticles; the color map represents the normalized number density of VORPAL-PD macroparticles. Electrons are injected only during periods of bubble expansion. A quasi-monoenergetic bunch is formed during Stage I and maintains its low-energy spread until dephasing, indicated by the group of early injected particles with $p_x \approx 0.5\,\mathrm{GeV}/c$. Groups of electrons encompassed by the ellipses were injected into the second and third buckets, to be further captured and accelerated by the expanding first bucket. Continuous injection during Stage II creates a polychromatic energy tail. (c) Collection volume: initial radial offsets ($R_{in} = \sqrt{y_{in}^2 + z_{in}^2}$) of electrons reaching dephasing limit vs. their initial longitudinal positions x_{in}. Black (red/grey) dots are CALDER-CIRC (VORPAL-PD) macroparticles. This collection volume indicates that the vast majority of electrons are collected from a hollow conical cylinder with a radius slightly smaller than the local bubble size.

The collection volume depicted in Fig. 1(c) indicates that the electrons are collected from a conical shell with a radius slightly smaller than the bubble radius. This structure of the collection volume indicates that the vast majority of trapped and accelerated electrons have impact parameters of sheath electrons (Tsung et al. 2006; Wu et al. 2009; Kalmykov et al. 2010; Pukhov et al. 2010; Kalmykov et al. 2011a, 2012). Collection volumes in the VORPAL-PD and CALDER-CIRC runs are almost identical during Stage I, whereas the radius of the cone is larger for VORPAL-PD during Stage II, on account of the greater expansion because of pulse diffraction.

Snapshots of electron density, longitudinal phase space, and energy spectra at the points of maximal expansion and contraction of the bubble are presented in Figs. 2–4. Data for panels (a), (b), and (c) in Figs. 2 and 3 are from the CALDER-CIRC simulation, and for panels (d), (e), and (f) are from the VORPAL-PD simulation.

The fully expanded bubble in the middle of Stage I is shown in Figs. 2(a) and (d). As soon as the bubble expands fully, injection terminates. Uninterrupted injection of sheath electrons before this point produces a large spread of longitudinal momentum and energy as shown in Figs. 3(a), (d), and 4(a).

A slight contraction of the bubble between $x = 0.95$ and 1.24 mm truncates the bunch. Electrons injected at the very end of the expansion interval are expelled, while particles remaining in the bucket are further accelerated. The transverse self-fields of the bunch are unable to prevent bucket contraction. Snapshots of the contracted bubble are presented in Figs. 2(b) and (e). During the contraction interval, the tail of the electron bunch, exposed to the highest accelerating gradient, equalises in energy with earlier injected electrons, producing a characteristic 'U' shape in the longitudinal phase space. This feature (also observed in the similar situation by Lu et al. 2007) is clearly seen in Figs. 3(b) and (e). As a result of this evolution, quasi-monoenergetic bunches are formed in both VORPAL-PD and CALDER-CIRC simulations at the end of Stage I. These

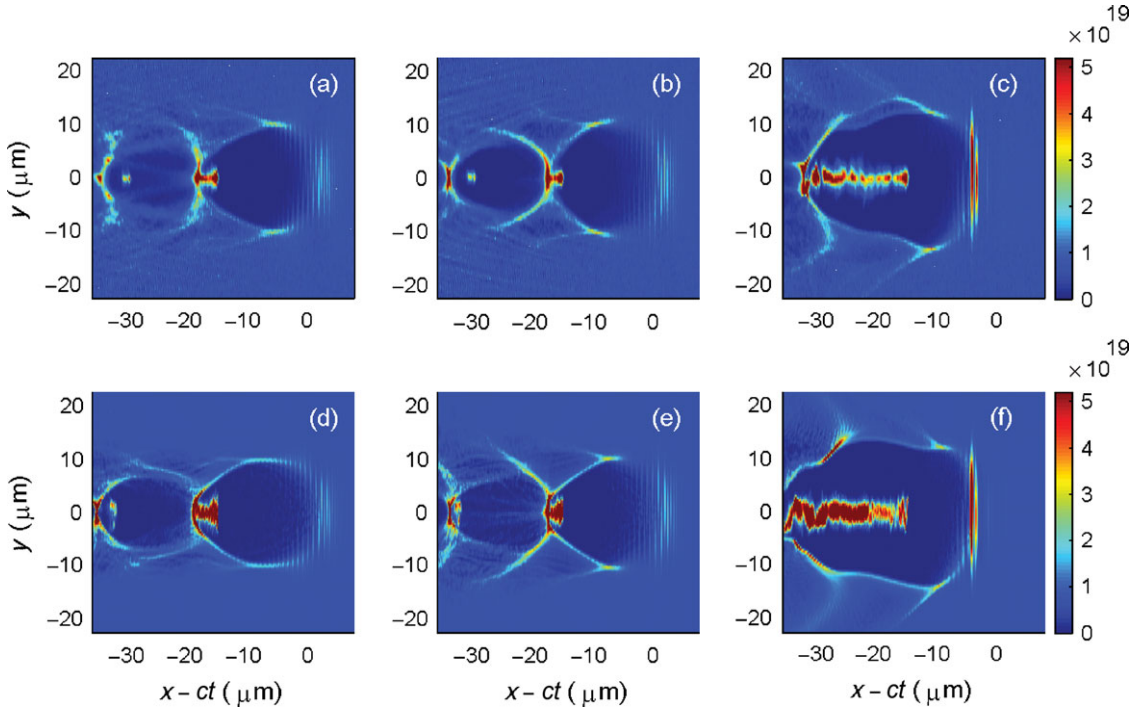

Figure 2. (Colour online) Electron density (in cm^{-3}) in the plane of laser polarization in CALDER-CIRC (top row) and VORPAL-PD simulations (bottom). Panels (a) and (d) show the fully expanded bubble in the middle of Stage I, (b) and (e) show the fully contracted bubble at the end of Stage I, and (c) and (f) show the bubble in the vicinity of electron dephasing point at the end of Stage II. $x = ct$ is the trajectory of the laser pulse maximum in vacuum; (a) and (d) correspond to the distance $x = ct \approx 930\,\mu m$ from the plasma edge, (b) and (e) correspond to $x = ct \approx 1210\,\mu m$, and (c) and (f) correspond to $x = ct \approx 2364\,\mu m$. Before the dephasing point, the bubble, elongated and deformed due to the laser pulse self-compression, traps considerable charge. Beam loading, however, is yet unable to terminate self-injection (cf. panels (c) and (f)).

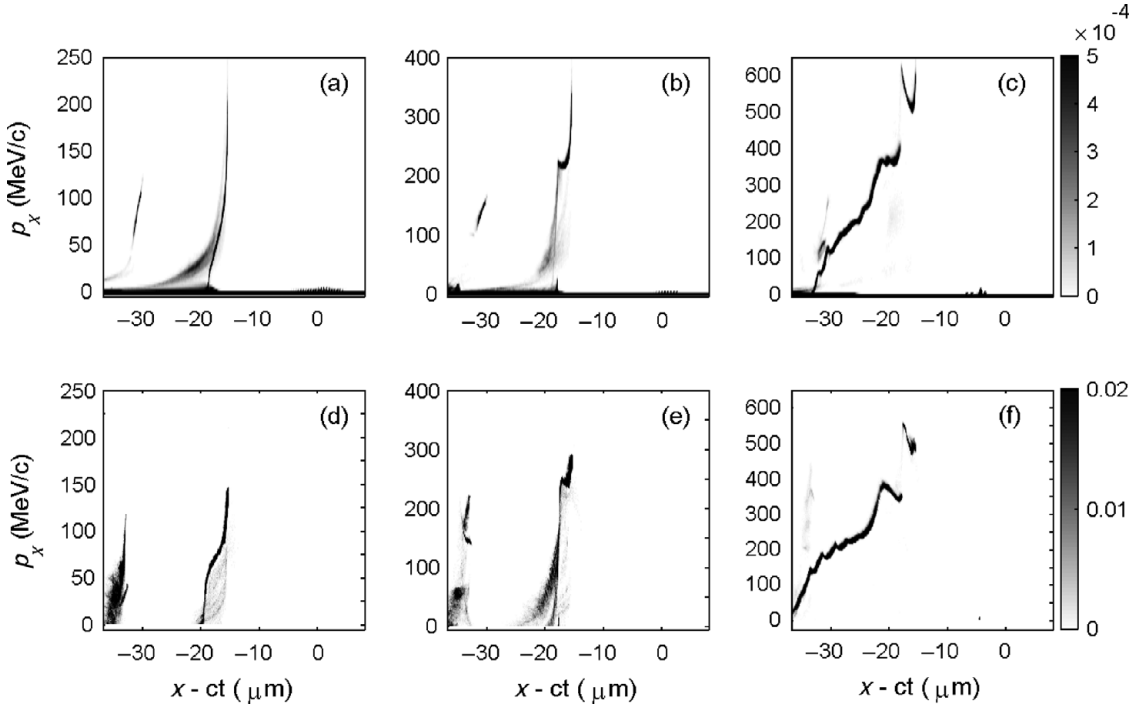

Figure 3. Electron density (arbitrary units) in longitudinal phase space in CALDER-CIRC (top row) and VORPAL-PD simulations (bottom). Each panel corresponds to the same panel of Fig. 2. Full expansion of the bubble saturates injection and initiates phase space rotation (panels (a) and (d)). Contraction of the bubble terminates injection, clipping the rear of the injected bunch, eliminating the low-energy tail. Phase space rotation makes the bunch quasi-monoenergetic (panels (b) and (e)). Elongation and deformation of the bubble because of the laser pulse self-compression causes continuous injection, producing an electron beam with a continuous spectrum of longitudinal momenta (panels (c) and (f)).

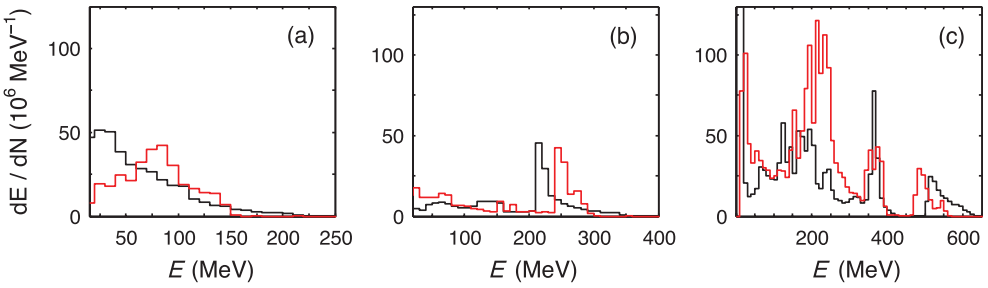

Figure 4. (Colour online) Electron energy spectra in CALDER-CIRC (black) and VORPAL-PD simulations (red/grey). Panels (a), (b), and (c) correspond to the phase space snapshots (a) and (d), (b) and (e), and (c) and (f) of Fig. 3, respectively. (a) At the point of full expansion, the electron energy spectrum is broad. (b) Full contraction of the bubble suppresses the low-energy tail and reduces the energy spread. Electrons from the second bucket contribute to the background, seen in the diffuse peaks around 150 MeV. (c) Continuous injection caused by bubble expansion and deformation produces a massive polychromatic tail. The leading bunch, at $E \approx 500$ MeV, reaches dephasing, but is still distinct from the tail.

Table 1. Parameters of the quasi-monoenergetic bunch ($E > 200$ MeV) at the end of Stage I (cf. the spectra in Fig. 4(b)). Q_{mono} is the charge in pC; E_{mono} is the energy corresponding to the spectral peak (in MeV); ΔE_{mono} is the absolute energy spread (FWHM) in MeV; $\varepsilon_{N,y}$ and $\varepsilon_{N,z}$ are the normalized transverse emittance (in mm mrad) in and out of the laser polarization plane, respectively.

	Q_{mono}	E_{mono}	ΔE_{mono}	$\varepsilon_{N,y}$	$\varepsilon_{N,z}$
CALDER-CIRC	214	215	20	6.87	7.08
VORPAL-PD	193	245	20	10.7	6.08

quasi-monoenergetic spikes with <10% energy spread can be seen in Fig. 4(b). In addition to the quasi-monoenergetic spikes, these energy spectra also reveal diffuse features near 150 MeV, corresponding to the electrons trapped in the second bucket; these particles can be seen in the snapshots of electron density as shown in Figs. 2(b) and (e). These electrons, however, never equalise in energy with the leading high-energy bunch.

Parameters of the bunches, summarized in Table 1, appear to be very similar. Normalized transverse emittances presented in this table are calculated according to the usual definition $\varepsilon_{N,i} = (m_e c)^{-1}[(\langle p_i^2\rangle - \langle p_i\rangle^2)(\langle r_i^2\rangle - \langle r_i\rangle^2) - (\langle p_i r_i\rangle - \langle r_i\rangle\langle p_i\rangle)^2]^{1/2}$, where $i = y$ and z correspond to the emittance in and out of polarization plane. The beam asymmetry is more pronounced in the VORPAL-PD simulation, presumably on account of the inclusion of the complete electromagnetic field, in contrast to just two poloidal modes in CALDER-CIRC.

Agreement between two codes worsens during Stage II. As has already been noted, the bubble expansion is larger in the VORPAL-PD simulation. As a result, the amount of continuously injected charge at the dephasing point (2.5 nC) is about 60% higher and the divergence of the continuously injected beam (80 mrad) is about twice that in the CALDER-CIRC simulation. The difference in charge can be easily inferred from Fig. 4(c). On the other hand, parameters of the leading bunches are in reasonable agreement with the central energy 485 ± 20 MeV in the VORPAL-PD run against 515 ± 25 MeV in the CALDER-CIRC run. In both simulations, the emittance of the quasi-monoenergic component increases by ~30% over its value at the end of Stage I. The lower energy of the leading bunch in the VORPAL-PD run can be explained by its earlier dephasing because of more rapid expansion of the bubble.

Both codes agree that the bubble not only elongates during Stage II but also becomes more and more asymmetric in the laser polarization plane. The 'pennant-like' bubble shape is responsible for massive off-axis injection, leading to the noticeable beam centroid oscillations in the laser polarization plane seen in Figs. 2(c) and (f). Such phenomenon has been observed in similar situations by others (Glinec et al. 2008). This violation of symmetry is a manifestation of carrier-envelope phase effects in the interaction of a relativistically intense, linearly polarized, few cycle piston with the plasma (Nerush and Kostyukov 2009). Conversely, in the plane orthogonal to the laser polarization, both bucket and beam remain perfectly symmetric (not shown). Surprisingly, the two poloidal radiation modes of CALDER-CIRC still capture the field evolution well. Inclusion of higher order modes should improve the situation. On the other hand, Figs. 2(c) and (f) indicate that electromagnetic solvers of both codes agree on the group velocity of the laser pulse even in the situation where the pulse shrinks down to less than two cycles and remains strongly relativistic. This means that (a) poloidal mode decomposition does not damage dispersion in the axial direction, and (b) the coarse grid and dispersion properties of VORPAL-PD are sufficient to describe well the extreme case of pulse spectral broadening to $\Delta\omega \sim \omega_0$ and compression to nearly a single cycle.

Examination of the bubble evolution and collection volumes (cf. Fig. 1), together with individual snapshots of electron density in coordinate and longitudinal phase space, indicate that in spite of great difference in algorithms, VORPAL-PD and CALDER-CIRC reproduce the same correlation between the evolution of the bubble and the self-injection of sheath electrons, and agree quantitatively on the parameters of quasi-monoenergetic beams produced by the oscillating bubble. Self-injection

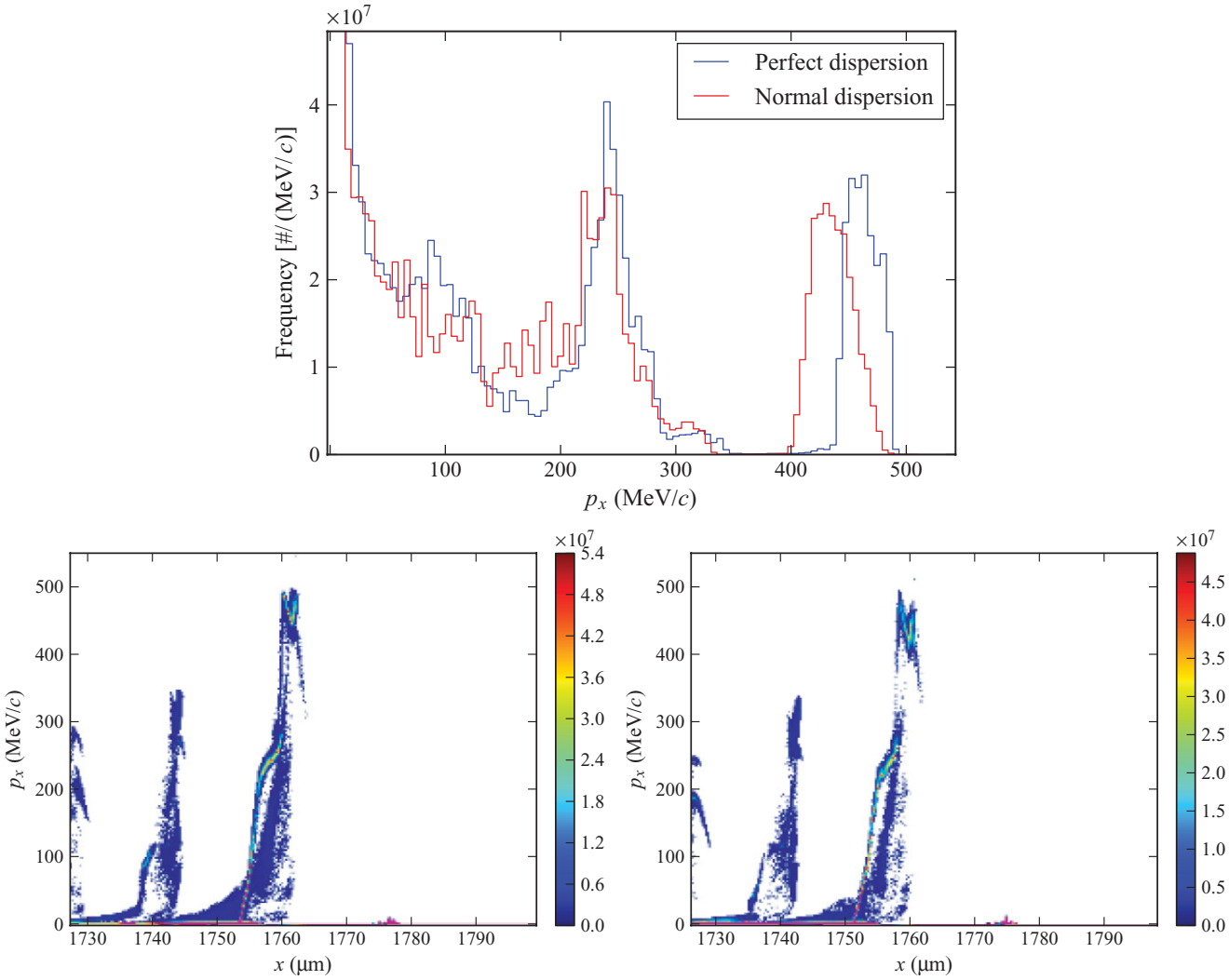

Figure 5. (Colour online) (Top) Electron longitudinal momentum spectra after 1.8 -mm propagation for perfect and normal dispersion. (Bottom) Longitudinal phase space for perfect dispersion (left) and normal dispersion (right).

begins, terminates, and resumes at exactly the same positions along the propagation axis in both runs, and electrons are collected from the same plasma volume. Despite differences in minor details, both codes consistently reproduce physical details of the self-injection process over the entire dephasing length. This level of agreement between very different numerical models indicates that the results are largely free of numerical artefacts. Importantly, the discrepancies emerge when the interaction develops noticeable non-cylindrically symmetric features, and hence the reduced field description of CALDER-CIRC loses precision. We believe that the agreement between the models may be improved in a straightforward fashion (viz. using a larger number of poloidal modes) without significantly reducing computational efficiency.

3.3. Effects of numerical dispersion control

As described above, simulating upcoming experiments will require economizing on computational cost as much as possible without sacrificing physical accuracy. One means of reducing longitudinal resolution requirements, and hence allowing a larger time step, is to minimize numerical dispersion through a modified electromagnetic update. Here we show how numerical dispersion quantitatively affects the injected electron bunch.

The immediate effect of numerical dispersion is an unphysically low group velocity of the laser pulse. While this effect is difficult to observe directly in the laser pulse because of more significant changes in the pulse shape, it can be seen in the electron phase space, which is of experimental importance. We examine the initially injected electrons at the point where they have rotated in phase space such that the beam has achieved minimal energy spread. The minimal energy spread condition is characterized by the phase space of the bunch being roughly longitudinally symmetric and in the shape of a 'U'. We find from the perfect dispersion simulation that this occurs after the laser has propagated approximately 1.8 mm into the plasma. We show longitudinal momentum spectra and phase space at this point for both perfect dispersion and normal dispersion in Fig. 5. We find that with the normal dispersion algorithm, the beam achieves lower energy and exhibits higher energy

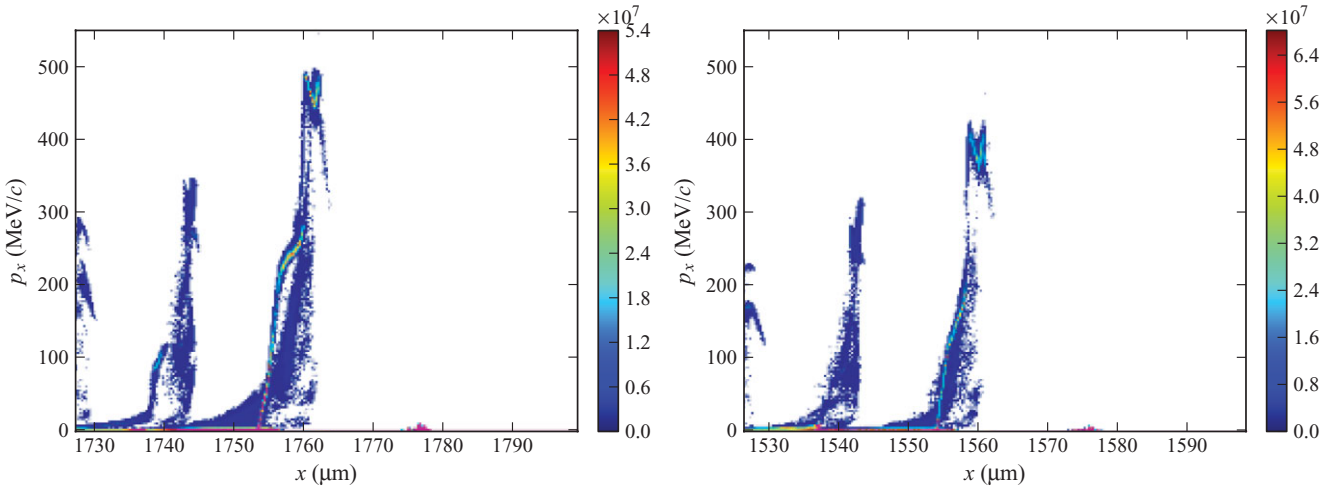

Figure 6. (Colour online) Longitudinal phase space for perfect dispersion (left) and normal dispersion (right) at the minimal energy spread point for both algorithms. For perfect dispersion, this is after 1.8 mm of propagation, and for normal dispersion after 1.6 mm.

spread than with the perfect dispersion algorithm. We also find that phase space rotation has occurred more quickly.

We also compare the two dispersion algorithms at points of minimal energy spread. Without dispersion control, the more rapid phase space rotation causes the minimal energy spread to occur after just 1.6 mm of propagation rather than 1.8 mm. We show the two phase space plots in Fig. 6. This comparison is relevant since for applications, one would want to design the system such that the injected beam exits the plasma at this point of minimum energy spread (Hafz et al. 2011). It is clear from these plots that with the normal dispersion algorithm, the beam has reached lower mean energy (390 MeV) at the minimum energy spread point than with perfect dispersion, where the beam has a mean energy of 460 MeV. In addition, the normal dispersion case exhibits slightly higher energy spread and total charge in the bunch.

We also compare the longitudinal momentum spectra and phase space at the points compared with CALDER-CIRC simulations in the previous section, namely 960 μm, 1.24 mm, and 2.4 mm. These comparisons are shown in Fig. 7. We can see, especially in the later two plots, that the injected bunch in the normal dispersion simulation shows both lower mean energy and greater phase space rotation than in the perfect dispersion run, and thus perfect dispersion agrees better with the CALDER-CIRC simulations as seen in the previous section.

While these discrepancies are small, they are noticeable and consistent with numerical group velocity error. As LPA system designs are refined, and diagnostics and control over the laser pulse and plasma improve, it will be important to control numerical effects on this level to optimize parameters through simulation. The perfect dispersion algorithm allows us to do so while still using low longitudinal resolution for computational efficiency.

4. Conclusions

In this paper we have demonstrated the utility of using computationally efficient, fully explicit 3D PIC codes to describe and explain the physical phenomena accompanying electron acceleration until dephasing in a self-guided LPA in the blowout regime. Electron self-injection and its relation to nonlinear dynamical processes involving the laser pulse and bubble were explored. Two approaches to reducing the computational cost of simulations were considered.

First, using the Cartesian code VORPAL with a newly developed perfect dispersion algorithm (Cowan et al. in preparation), VORPAL-PD, made it possible to use large grid spacings (∼15 grid points per wavelength in the direction of propagation) and proportionally larger time steps. This approach reproduces the correct group velocity of a broad bandwidth laser pulse. The red-shift, self-compression, and depletion of the laser pulse were thus described correctly, with proper resolution of all important physical scales.

Second, the well-preserved axial symmetry of the problem allowed us to use a reduced geometry description, with poloidal-mode decomposition of currents and fields. This approach was realized in the code CALDER-CIRC (Lifschitz et al. 2009). By using only two modes, we approached the performance of a 2D code, at the same time preserving the correct cylindrical geometry of the interaction. The high computational efficiency of CALDER-CIRC allowed us to use a very high longitudinal resolution (∼50 grid points per laser wavelength in the direction of propagation) and a large number of macro-particles (∼50 per cylindrical cell), eliminating numerical dispersion and strongly reducing the sampling noise. This high resolution simulation did not indicate any new physical effects relative to the VORPAL-PD runs, and did not exhibit significant differences in quantitative results. Even with strong violation of cylindrical symmetry (such as near the dephasing limit, when oscillations of the

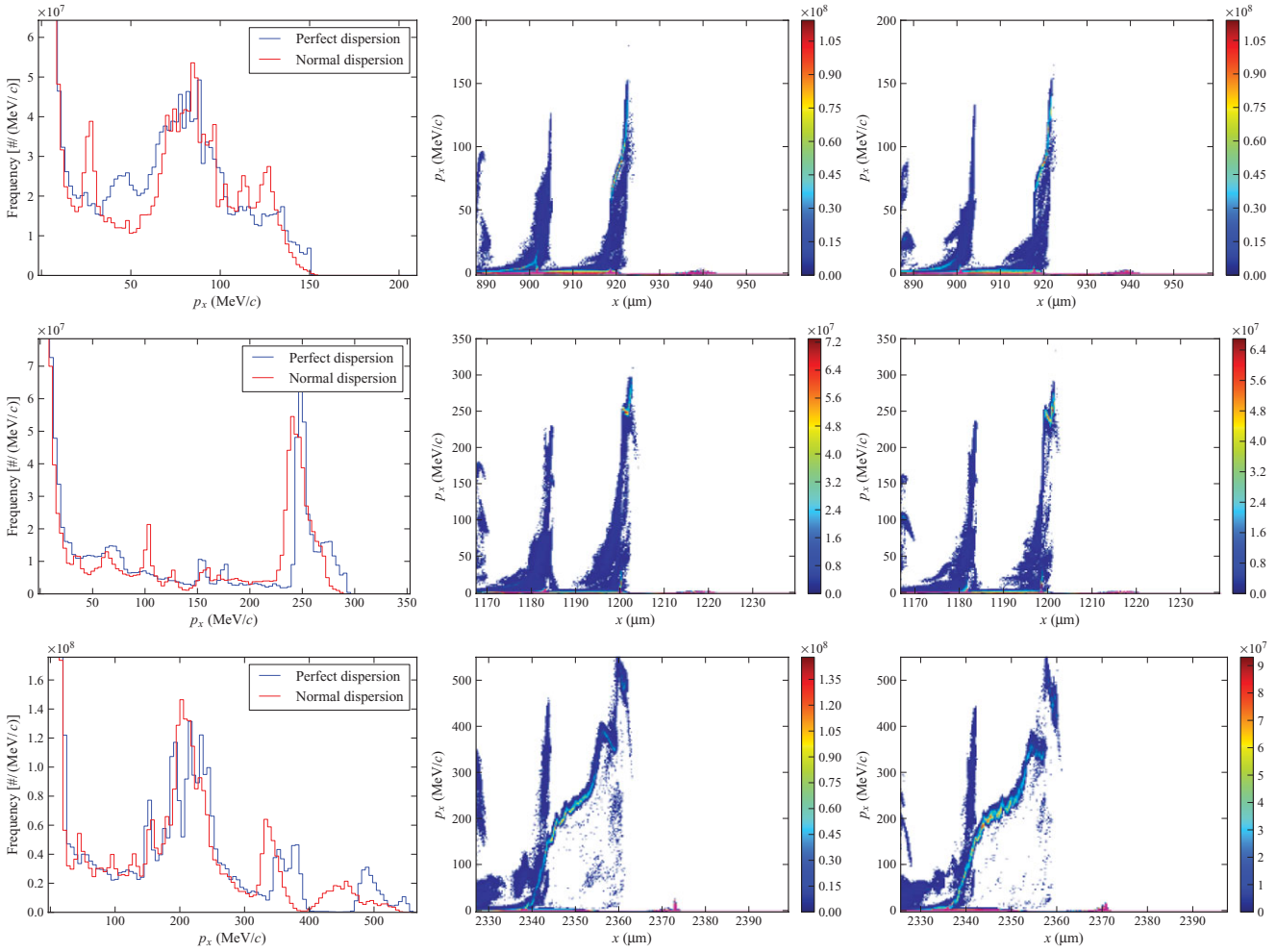

Figure 7. (Colour online) Comparisons of longitudinal momentum and phase space. Momentum spectra for perfect and normal dispersion (left), the perfect dispersion phase space (center), and the normal dispersion phase space (right). The top row shows electron distribution at 960 μm of propagation, the middle row at 1.24 mm, and the bottom row at 2.4 mm of propagation.

beam centroid are apparent), the CALDER-CIRC results remained qualitatively correct.

Both codes described precisely the self-focusing of the laser pulse, the oscillations of its spot size, and related oscillations of the bubble; electron self-injection into the oscillating bubble and formation of a quasi-monoenergetic bunch; laser pulse frequency broadening and self-compression into the relativistic piston; constant elongation of the bubble during the piston formation; and uninterrupted electron injection eventually overloading the bubble. The codes showed excellent agreement on the locations of initiation and extinction of injection, on the collection volume, and on parameters of the quasi-monoenergetic component in the electron spectrum, indicating that the results are free of numerical artefacts. It is especially interesting that the CALDER-CIRC simulation with just two poloidal modes did not lose accuracy and preserved the correct group velocity (agreeing with the VORPAL-PD run) even when the laser pulse was compressed down to two cycles.

We thus conclude that (1) using perfect dispersion, taking a coarser grid and larger time steps, and using higher order splines for macroparticle shapes to suppress the sampling noise, or (2) neglecting high-order non-axisymmetric field and current components, thus reducing the dimensionality of the problem are both effective and promising means to increase the computational efficiency without sacrificing fidelity. Both of these methods are applicable to the design of upcoming experiments on GeV-scale acceleration of electrons with 100-TW-scale lasers.

Acknowledgements

The work of B.M.C. and D.L.B. was partially supported by U.S. DOE Contracts DE-SC0006245 (SBIR) and DE-FC02-07ER41499 (SciDAC). The work of S.Y.K. and B.A.S. was partially supported by U.S. DOE Contracts DE-FG02-08ER55000 and DE-FG02-05ER15663, NSF Grant PHY-1104683, DTRA Contract HDTRA1-11-C-0001, and AFOSR Grants FA9550-11-1-0157 and 9550-08-1-0232. X.D. and A.F.L. thank Victor Malka for his support during the development of CALDER-CIRC. A.B. and E.L. acknowledge the support

of LASERLAB-EUROPE/LAPTECH through EC FP7 contract No. 228334. The CALDER-CIRC simulations in this work were performed using high-performance computing resources of CCRT made available by GENCI (grant 2011-056304). VORPAL simulations used resources of the National Energy Research Scientific Computing Center, which is supported by the Office of Science of the U.S. DOE under Contract No. DE-AC02-05CH11231.

References

Andreev, N. E., Gorbunov, L. M., Mora, P. and Ramazashvili, R. R. 2007 Filamentation of ultrashort laser pulses propagating in tenuous plasmas. *Phys. Plasmas* **14**, 083104.

Birdsall, C. K. and Langdon, A. B. 1985 *Plasma Physics via Computer Simulation*. New York, NY: McGraw-Hill.

Cipiccia, S., Islam, M. R., Ersfeld, B., Shanks, R. P., Brunetti, E., Vieux, G., Yang, X., Issac, R. C., Wiggins, S. M., Welsh, G. H. et al. 2011 Gamma-rays from harmonically resonant betatron oscillations in a plasma wake. *Nat. Phys.* **7**, 867–871.

Clayton, C. E., Ralph, J. E., Albert, F., Fonseca, R. A., Glenzer, S. H., Joshi, C., Lu, W., Marsh, K. A., Martins, S. F., Mori, W. B. et al. 2010 Self-guided laser wakefield acceleration beyond 1 GeV using ionization-induced injection. *Phys. Rev. Lett.* **105**, 105003.

Cormier-Michel, E., Shadwick, B. A., Geddes, C. G. R., Esarey, E., Schroeder, C. B. and Leemans, W. P. 2008 Unphysical kinetic effects in particle-in-cell modeling of laser wakefield accelerators. *Phys. Rev.* E **78**(1), 016404.

Courant, R., Friedrichs, K. and Lewy, H. 1967 On the partial difference equations of mathematical physics. *IBM J. Res. Develop.* **11**, 215–234.

Cowan, B. M., Bruhwiler, D. L., Cary, J. R., Cormier-Michel, E., Esarey, E. and Geddes, C. G. R. in preparation Generalized algorithm for control of numerical dispersion in explicit time-domain electromagnetic simulations.

Cummings, P. and Thomas, A. G. R. 2011 A computational investigation of the impact of aberrated Gaussian laser pulses on electron beam properties in laser-wakefield acceleration experiments. *Phys. Plasmas* **18**, 053110.

Esarey, E., Schroeder, C. B. and Leemans, W. P. 2009 Physics of laser-driven plasma-based electron accelerators. *Rev. Mod. Phys.* **81**(3), 1229–1285.

Faure, J., Glinec, Y., Pukhov, A., Kiselev, S., Gordienko, S., Lefebvre, E., Rousseau, J.-P., Burgy, F. and Malka, V. 2004 A laser-plasma accelerator producing monoenergetic electron beams. *Nature* **431**, 541.

Faure, J., Glinec, Y., Santos, J. J., Ewald, F., Rousseau, J.-P., Kiselev, S., Pukhov, A., Hosokai, T. and Malka, V. 2005 Observation of laser-pulse shortening in nonlinear plasma waves. *Phys. Rev. Lett.* **95**, 205003.

Fourmaux, S., Corde, S., Phuoc, K. T., Lassonde, P., Lebrun, G., Payeur, S., Martin, F., Sebban, S., Malka, V., Rousse, A. et al. 2011 Single shot phase contrast imaging using laser-produced betatron x-ray beams. *Opt. Lett.* **36**, 2426–2428.

Froula, D. H., Clayton, C. E., Döppner, T., Marsh, K. A., Barty, C. P. J., Divol, L., Fonseca, R. A., Glenzer, S. H., Joshi, C., Lu, W. et al. 2009 Measurements of the critical power for self-injection of electrons in a laser wakefield accelerator. *Phys. Rev. Lett.* **103**, 215006.

Fuchs, M., Weingartner, R., Popp, A., Major, Z., Becker, S., Osterhoff, J., Cortrie, I., Zeitler, B., Hörlein, R., Tsakiris, G. D. et al. 2009 Laser-driven soft X-ray undulator source. *Nat. Phys.* **5**, 826–829.

Geddes, C. G. R., Toth, Cs., van Tilborg, J., Esarey, E., Schroeder, C. B., Bruhwiler, D. L., Nieter, C., Cary, J. R. and Leemans, W.P. 2004 High-quality electron beams from a laser wakefield accelerator using plasma-channel guiding. *Nature* **431**, 538.

Glinec, Y., Faure, J., Lifschitz, A., Vieira, J. M., Fonseca, R A., Silva, L. O. and Malka, V. 2008 Direct observation of betatron oscillations in a laser-plasma electron accelerator. *Europhys. Lett.* **81**, 64001.

Gorbunov, L. M., Kalmykov, S. Y. and Mora, P. 2005 Laser wakefield acceleration by petawatt ultrashort laser pulses. *Phys. Plasmas* **12**, 033101.

Gorbunov, L. M. and Kirsanov, V. I. 1987 Excitation of plasma waves by an electromagnetic wave packet. *Sov. Phys. JETP* **66**, 290–294.

Gordienko, S. and Pukhov, A. 2005 Scalings for ultrarelativistic laser plasmas and quasimonoenergetic electrons. *Phys. Plasmas* **12**(4), 043109.

Grüner, F., Becker, S., Schramm, U., Eichner, T., Fuchs, M., Weingartner, R., Habs, D., Meyer-ter-Vehn, J., Geissler, M., Ferrario, M. et al. 2007 Design considerations for table-top, laser-based VUV and X-ray free electron lasers. *Appl. Phys.* B **86**(3), 431–435.

Hafz, N. A. M., Jeong, T. M., Choi, I. W., Lee, S. K., Pae, K. H., Kulagin, V. V., Sung, J. H., Yu, T. J., Hong, K.-H., Hosokai, T. et al. 2008 Stable generation of GeV-class electron beams from self-guided laser-plasma channels. *Nat. Photonics* **2**(9), 571–577.

Hafz, N. A. M., Lee, S. K., Jeong, T. M. and Lee, J. 2011 Evolution of self-injected quasi-monoenergetic electron beams in a plasma bubble. *Nucl. Instrum. Methods* A **637**, S51–S53.

Hartemann, F. V., Gibson, D. J., Brown, W. J., Rousse, A., Ta Phuoc, K., Malka, V., Faure, J. and Pukhov, A. 2007 Compton scattering x-ray sources driven by laser wakefield acceleration. *Phys. Rev. ST Accel. Beams* **10**(1), 011301.

Hidding, B., Königstein, T., Will, O., Rosenzweig, J. B., Nakajima, K. and Pretzler, G. 2011 Laser-plasma-accelerators – a novel, versatile tool for space radiation studies. *Nucl. Instrum. Methods* A **636**, 31–40.

Hockney, R. W. and Eastwood, J. W. 1981 *Computer Simulation Using Particles*. New York, NY: McGraw-Hill.

Kalmykov, S. Y., Beck, A., Davoine, X., Lefebvre, E. and Shadwick, B. A. 2012 Laser plasma acceleration with a negatively chirped pulse: all-optical control over dark current in the blowout regime. *New J. Phys.* **14**(3), 033025.

Kalmykov, S. Y., Beck, A., Yi, S. A., Khudik, V. N., Downer, M. C., Lefebvre, E., Shadwick, B. A. and Umstadter, D. P. 2011a Electron self-injection into an evolving plasma bubble: quasi-monoenergetic laser-plasma acceleration in the blowout regime. *Phys. Plasmas* **18**(5), 056704.

Kalmykov, S. Y., Shadwick, B. A., Beck, A. and Lefebvre, E. 2011b Physics of quasi-monoenergetic laser-plasma acceleration of electrons in the blowout regime. In: *Femtosecond-Scale Optics* (ed. A. V. Andreev), pp. 113–138. Croatia: InTech.

Kalmykov, S. Y., Yi, S. A., Beck, A., Lifschitz, A. F., Davoine, X., Lefebvre, E., Khudik, V., Shvets, G. and Downer, M. C. 2011c Dark-current-free petawatt laser-driven wakefield accelerator based on electron self-injection

into an expanding plasma bubble. *Plasma Phys. Control. Fusion* **53**, 014006.

Kalmykov, S. Y., Yi, S. A., Beck, A., Lifschitz, A. F., Davoine, X., Lefebvre, E., Pukhov, A., Khudik, V., Shvets, G., Reed, S. A. et al. 2010 Numerical modelling of a 10-cm-long multi-GeV laser wakefield accelerator driven by a self-guided petawatt pulse. *New J. Phys.* **12**(4), 045019.

Kalmykov, S., Yi, S. A., Khudik, V. and Shvets, G. 2009 Electron self-injection and trapping into an evolving plasma bubble. *Phys. Rev. Lett.* **103**(13), 135004.

Kärkkäinen, M., Gjonaj, E., Lau, T. and Weiland, T. 2006 Low-dispersion wake field calculation tools. In *Proceedings of the 2006 International Computational Accelerator Physics Conference*, Chamonix, France, 2006, pp. 35–40.

Karsch, S., Osterhoff, J., Popp, A., Rowlands-Rees, T. P., Major, Zs., Fuchs, M., Marx, B., Hörlein, R., Schmid, K., Veisz, L. et al. 2007 GeV-scale electron acceleration in a gas-filled capillary discharge waveguide. *New J. Phys.* **9**(11), 415.

Kneip, S., McGuffey, C., Dollar, F., Bloom, M. S., Chvykov, V., Kalintchenko, G., Krushelnick, K., Maksimchuk, A., Mangles, S. P. D., Matsuoka, T. et al. 2011 X-ray phase contrast imaging of biological specimens with femtosecond pulses of betatron radiation from a compact laser plasma wakefield accelerator. *Appl. Phys. Lett.* **99**, 093701.

Kneip, S., McGuffey, C., Martins, J. L., Martins, S. F., Bellei, C., Chvykov, V., Dollar, F., Fonseca, R., Huntington, C., Kalintchenko, G. et al. 2010 Bright spatially coherent synchrotron x-rays from a table-top source. *Nat. Phys.* **6**, 980–983.

Kneip, S., Nagel, S. R., Martins, S. F., Mangles, S. P. D., Bellei, C., Chekhlov, O., Clarke, R. J., Delerue, N., Divall, E. J., Doucas, G. et al. 2009 Near-GeV acceleration of electrons by a nonlinear plasma wave driven by a self-guided laser pulse. *Phys. Rev. Lett.* **103**, 035002.

Leemans, W. P., Esarey, E., van Tilborg, J., Michel, P. A., Schroeder, C. B., Toth, C., Geddes, C. G. R. and Shadwick, B. A. 2005 Radiation from laser accelerated electron bunches: coherent terahertz and femtosecond x-rays. *IEEE Trans. Plasma Science* **33**(1), 8–22.

Leemans, W. P., Nagler, B., Gonsalves, A. J., Toth, Cs., Nakamura, K., Geddes, C. G. R., Esarey, E., Schroeder, C. B. and Hooker, S. M. 2006 GeV electron beams from a centimetre-scale accelerator. *Nat. Phys.* **2**(10), 696–699.

Leemans, W. P., Rodgers, D., Catravas, P. E., Geddes, C. G. R., Fubiani, G., Esarey, E., Shadwick, B. A., Donahue, R. and Smith, A. 2001 Gamma-neutron activation experiments using laser wakefield accelerators. *Phys. Plasmas* **8**, 2510–2516.

Lifschitz, A. F., Davoine, X., Lefebvre, E., Faure, J., Rechatin, C. and Malka, V. 2009 Particle-in-cell modelling of laser-plasma interaction using Fourier decomposition. *J. Comput. Phys.* **228**(5), 1803–1814.

Liu, J. S., Xia, C. Q., Wang, W. T., Lu, H. Y., Wang, Ch., Deng, A. H., Li, W. T., Zhang, H., Liang, X. Y., Leng, Y. X. et al. 2011 All-optical cascaded laser wakefield accelerator using ionization-induced injection. *Phys. Rev. Lett.* **107**, 035001.

Lontano, M. and Murusidze, I. G. 2003 Dynamics of space-time self-focusing of a femto-second relativistic laser pulse in an underdense plasma. *Opt. Express* **11**, 248–258.

Lu, W., Huang, C., Zhou, M., Tzoufras, M., Tsung, F. S., Mori, W. B. and Katsouleas, T. 2006 A nonlinear theory for multidimensional relativistic plasma wave wakefields. *Phys. Plasmas* **13**, 056709.

Lu, H., Liu, M., Wang, W., Wang, C., Liu, J., Deng, A., Xu, J., Xia, C., Li, W., Zhang, H. et al. 2011 Laser wakefield acceleration of electron beams beyond 1 GeV from an ablative capillary discharge waveguide. *Appl. Phys. Lett.* **99**, 091502.

Lu, W., Tzoufras, M., Joshi, C., Tsung, F. S., Mori, W. B., Vieira, J., Fonseca, R. A. and Silva, L. O. 2007 Generating multi-GeV electron bunches using single stage laser wakefield acceleration in a 3D nonlinear regime. *Phys. Rev. ST Accel. Beams* **10**(6), 061301.

Maksimchuk, A., Reed, S., Bulanov, S. S., Chvykov, V., Kalintchenko, G., Matsuoka, T., McGuffey, C., Mourou, G., Naumova, N., Nees, J. et al. 2008 Studies of laser wakefield structures and electron acceleration in underdense plasmas. *Phys. Plasmas* **15**, 056703.

Mangles, S. P. D., Genoud, G., Kneip, S., Burza, M., Cassou, K., Cros, B., Dover, N. P., Kamperidis, C., Najmudin, Z., Persson, A. et al. 2009 Controlling the spectrum of x-rays generated in a laser-plasma accelerator by tailoring the laser wavefront. *Appl. Phys. Lett.* **95**, 181106.

Mangles, S. P. D., Murphy, C. D., Najmudin, Z., Thomas, A. G. R., Collier, J. L., Dangor, A. E., Divall, E. J., Foster, P. S., Gallacher, J. G., Hooker, C. J. et al. 2004 Monoenergetic beams of relativistic electrons from intense laser-plasma interactions. *Nature* **431**, 535.

Mangles, S. P. D., Thomas, A. G. R., Lundh, O., Lindau, F., Kaluza, M. C., Persson, A., Wahlström, C.-G., Krushelnick, K. and Najmudin, Z. 2007 On the stability of laser wakefield electron accelerators in the monoenergetic regime. *Phys. Plasmas* **14**(5), 056702.

Martins, S. F., Fonseca, R. A., Lu, W., Mori, W. B. and Silva, L. O. 2010 Exploring laser-wakefield-accelerator regimes for near-term lasers using particle-in-cell simulation in Lorentz-boosted frames. *Nat. Phys.* **6**, 311.

Mora, P. and Antonsen, Jr., T. M. 1996 Electron cavitation and acceleration in the wake of an ultraintense, self-focused laser pulse. *Phys. Rev.* E **53**, R2068–R2071.

Nerush, E. N. and Kostyukov, I. Y. 2009 Carrier-envelope phase effects in plasma-based electron acceleration with few-cycle laser pulses. *Phys. Rev. Lett.* **103**, 035001.

Nieter, C. and Cary, J. R. 2004 VORPAL: a versatile plasma simulation code. *J. Comput. Phys.* **196**, 538.

Oguchi, A., Zhidkov, A., Takano, K., Hotta, E., Nemoto, K. and Nakajima, K. 2008 Multiple self-injection in the acceleration of monoenergetic electrons by a laser wake field. *Phys. Plasmas* **15**, 043102.

Pai, C.-H., Chang, Y.-Y., Ha, L.-C., Xie, Z.-H., Lin, M.-W., Lin, J.-M., Chen, Y.-M., Tsaur, G., Chu, H.-H., Chen, S.-H. et al. 2010 Generation of intense ultrashort mid-infrared pulses by laser-plasma interaction in the bubble regime. *Phys. Rev.* A **82**, 063804.

Pollock, B. B., Clayton, C. E., Ralph, J. E., Albert, F., Davidson, A., Divol, L., Filip, C., Glenzer, S. H., Herpoldt, K., Lu, W. et al. 2011 Demonstration of a narrow energy spread, ~0.5 GeV electron beam from a two-stage laser wakefield accelerator. *Phys. Rev. Lett.* **107**, 045001.

Popp, A., Vieira, J., Osterhoff, J., Major, Zs., Hörlein, R., Fuchs, M., Weingartner, R., Rowlands-Rees, T. P., Marti, M., Fonseca, R. A. et al. 2010 All-optical steering of laser-wakefield-accelerated electron beams. *Phys. Rev. Lett.* **105**, 215001.

Pukhov, A. 1999 Three-dimensional electromagnetic relativistic particle-in-cell code VLPL (Virtual Laser Plasma Lab). *J. Plasma Phys.* **61**(03), 425–433.

Pukhov, A., an der Brügge, D. and Kostyukov, I. 2010 Relativistic laser plasmas for electron acceleration and short wavelength radiation generation. *Plasma Phys. Control. Fusion* **52**, 124039.

Pukhov, A. and Meyer-ter-Vehn, J. 2002 Laser wakefield acceleration: the highly non-linear broken-wave regime. *Appl. Phys.* B **74**, 355–361.

Ramanathan, V., Banerjee, S., Powers, N., Cunningham, N., Chandler-Smith, N. A., Zhao, K., Brown, K., Umstadter, D., Clarke, S., Pozzi, S. et al. 2010 Submillimeter-resolution radiography of shielded structures with laser-accelerated electron beams. *Phys. Rev. ST Accel. Beams* **13**, 104701.

Reed, S. A., Chvykov, V., Kalintchenko, G., Matsuoka, T., Yanovsky, V., Vane, C. R., Beene, J. R., Stracener, D., Schultz, D. R. and Maksimchuk, A. 2007 Efficient initiation of photonuclear reactions using quasimonoenergetic electron beams from laser wakefield acceleration. *J. Appl. Phys.* **102**, 073103.

Rosenzweig, J. B., Breizman, B., Katsouleas, T. and Su, J. J. 1991 Acceleration and focusing of electrons in two-dimensional nonlinear plasma wake fields. *Phys. Rev.* A **44**, R6189–R6192.

Rousse, A., Ta Phuoc, K., Shah, R., Fitour, R. and Albert, F. 2007 Scaling of betatron X-ray radiation. *Eur. Phys. J.* D **45**, 391–398.

Rousse, A., Ta Phuoc, K., Shah, R., Pukhov, A., Lefebvre, E., Malka, V., Kiselev, S., Burgy, F., Rousseau, J.-P., Umstadter, D. et al. 2004 Production of a keV X-ray beam from synchrotron radiation in relativistic laser-plasma interaction. *Phys. Rev. Lett.* **93**(13), 135005.

Schlenvoigt, H.-P., Haupt, K., Debus, A., Budde, F., Jäckel, O., Pfotenhauer, S., Gallacher, J. G., Brunetti, E., Shanks, R. P., Wiggins, S. M., et al. 2008b Synchrotron radiation from laser-accelerated monoenergetic electrons. *IEEE Trans. Plasma Sci.* **36**(4), 1773–1781.

Schlenvoigt, H.-P., Haupt, K., Debus, A., Budde, F., Jäckel, O., Pfotenhauer, S., Schwoerer, H., Rohwer, E., Gallacher, J. G., Brunetti, E. et al. 2008a A compact synchrotron radiation source driven by a laser-plasma wakefield accelerator. *Nat. Phys.* **4**(2), 130–133.

Sprangle, P., Esarey, E. and Ting, A. 1990 Nonlinear interaction of intense laser pulses in plasmas. *Phys. Rev.* A **41**(8), 4463–4469.

Sun, G.-Z., Ott, E., Lee, Y. C. and Guzdar, P. 1987 Self-focusing of short intense pulses in plasmas. *Phys. Fluids* **30**, 526–532.

Ta Phuoc, K., Burgy, F., Rousseau, J.-P., Malka, V., Rousse, A., Shah, R., Umstadter, D., Pukhov, A. and Kiselev, S. 2005 Laser-based synchrotron radiation. *Phys. Plasmas* **12**(2), 023101.

Taflove, A. and Hagness, S. C. 2005 *Computational Electrodynamics: The Finite-Difference Time-Domain Method*, 3rd edn. Boston, MA: Artech House.

Tajima, T. and Dawson, J. M. 1979 Laser electron accelerator. *Phys. Rev. Lett.* **43**(4), 267–270.

Thomas, A. G. R., Mangles, S. P. D., Murphy, C. D., Dangor, A. E., Foster, P. S., Gallacher, J. G., Jaroszynski, D. A., Kamperidis, C., Krushelnick, K., Lancaster, K. L., et al. 2009 Ultrashort pulse filamentation and monoenergetic electron beam production in LWFAs. *Plasma Phys. Control. Fusion* **51**, 024010.

Thomas, A. G. R., Najmudin, Z., Mangles, S. P. D., Murphy, C. D., Dangor, A. E., Kamperidis, C., Lancaster, K. L., Mori, W. B., Norreys, P. A., Rozmus, W. et al. 2007 Effect of laser-focusing conditions on propagation and monoenergetic electron production in laser-wakefield accelerators. *Phys. Rev. Lett.* **98**(9), 095004.

Tsung, F. S., Lu, W., Tzoufras, M., Mori, W. B., Joshi, C., Vieira, J. M., Silva, L. O. and Fonseca, R. A. 2006 Simulation of monoenergetic electron generation via laser wakefield accelerators for 5–25 TW lasers. *Phys. Plasmas* **13**(5), 056708.

Tsung, F. S., Ren, C., Silva, L. O., Mori, W. B. and Katsouleas, T. 2002 Generation of ultra-intense single-cycle laser pulses by using photon deceleration. *Proc. Natl. Acad. Sci. USA.* **99**, 29–32.

Vay, J.-L., Geddes, C. G. R., Cormier-Michel, E. and Grote, D. P. 2011 Numerical methods for instability mitigation in the modeling of laser wakefield accelerators in a Lorentz-boosted frame. *J. Comput. Phys.* **230**(15), 5908–5929.

Vieira, J., Fiúza, F., Silva, L. O., Tzoufras, M. and Mori, W. B. 2010 Onset of self-steepening of intense laser pulses in plasmas. *New J. Phys.* **12**, 045025.

Wiggins, S. M., Issac, R. C., Welsh, G. H., Brunetti, E., Shanks, R. P., Anania, M. P., Cipiccia, S., Manahan, G. G., Aniculaesei, C., Ersfeld, B. et al. 2010 High quality electron beams from a laser wakefield accelerator. *Plasma Phys. Control. Fusion* **52**, 124032.

Wu, H.-C., Xie, B.-S., Liu, M.-P., Hong, X.-R., Zhang, S. and Yu, M. Y. 2009 Electron trajectories and betatron oscillation in the wake bubble in laser-plasma interaction. *Phys. Plasmas* **16**, 073108.

Xu, H., Yu, W., Lu, P., Senecha, V. K., He, F., Shen, B., Qian, L., Li, R. and Xu, Z. 2005 Electron self-injection and acceleration driven by a tightly focused intense laser beam in an underdense plasma. *Phys. Plasmas* **12**, 013105.

Yanovsky, V., Chvykov, V., Kalinchenko, G., Rousseau, P., Planchon, T., Matsuoka, T., Maksimchuk, A., Nees, J., Cheriaux, G., Mourou, G. et al. 2008 Ultra-high intensity 300-TW laser at 0.1 Hz repetition rate. *Opt. Express* **16**, 2109–2114.

Yee, K. S. 1966 Numerical solution of initial boundary value problems involving Maxwell's equations in isotropic media. *IEEE Trans. Antennas Propag.* **14**(3), 302–307.

Zagorodnov, I., Schuhmann, R. and Weiland, T. 2003 Long-time numerical computation of electromagnetic fields in the vicinity of a relativistic source. *J. Comput. Phys.* **191**, 525–541.

Zagorodnov, I. and Weiland, T. 2005 TE/TM field solver for particle beam simulations without numerical Cherenkov radiation. *Phys. Rev. ST Accel. Beams* **8**(4), 042001.

Zhidkov, A., Koga, J., Hosokai, T., Fujii, T., Oishi, Y., Nemoto, K. and Kodama, R. 2010 Characterization of electron self-injection in laser wakefield acceleration due to the parametric resonance. *Phys. Plasmas* **17**, 083101.